Received 24 November 2007
Revised 4 May 2008
Accepted 12 May 2008

Simulation of laminar flow in a three-dimensional lid-driven cavity by lattice Boltzmann method

Santanu De
Department of Aerospace Engineering, Indian Institute of Science, Bangalore, India
K. Nagendra
National Institute of Technology Karnataka, Surathkal, India, and Department of Aerospace Engineering, Indian Institute of Science, Bangalore, India, and
K.N. Lakshmisha
Department of Aerospace Engineering, Indian Institute of Science, Bangalore, India

Abstract

Purpose – The purpose of this paper is to apply lattice Boltzmann equation method (LBM) with multiple relaxation time (MRT) model, to investigate lid-driven flow in a three-dimensional (3D), rectangular cavity, and compare the results with flow in an equivalent two-dimensional (2D) cavity.
Design/methodology/approach – The second-order MRT model is implemented in a 3D LBM code. The flow structure in cavities of different aspect ratios (0.25-4) and Reynolds numbers (0.01-1000) is investigated. The LBM simulation results are compared with those from numerical solution of Navier-Stokes (NS) equations and with available experimental data.
Findings – The 3D simulations demonstrate that 2D models may predict the flow structure reasonably well at low Reynolds numbers, but significant differences with experimental data appear at high Reynolds numbers. Such discrepancy between 2D and 3D results are attributed to the effect of boundary layers near the side-walls in transverse direction (in 3D), due to which the vorticity in the core-region is weakened in general. Secondly, owing to the vortex stretching effect present in 3D flow, the vorticity in the transverse plane intensifies whereas that in the lateral plane decays, with increase in Reynolds number. However, on the symmetry-plane, the flow structure variation with respect to cavity aspect ratio is found to be qualitatively consistent with results of 2D simulations. Secondary flow vortices whose axis is in the direction of the lid-motion are observed; these are weak at low Reynolds numbers, but become quite strong at high Reynolds numbers.
Originality/value – The findings will be useful in the study of variety of enclosed fluid flows.

Keywords Laminar flow, Flow, Modelling, Fluid dynamics
Paper type Research paper

1. Introduction

Viscous recirculating flow in a wall-bounded cavity, driven by steady, tangential, linear translation of its lid is an excellent setup for studying many fundamental phenomena of incompressible flows with or without heat transfer, such as corner vortices, longitudinal vortices, Taylor-Görtler-like (TGL) vortices, transition and turbulence (Shankar and Deshpande, 2000; Shuja *et al.*, 2000; Das and Kanna, 2007; Wong 2007). Furthermore, this type of flow is encountered in numerous practical applications, e.g. short-dwell coaters and flexible coaters used for production of high-grade papers and photographic films (Aidun *et al.*, 1991), mixing of the fluids (Jana *et al.*, 1994) and in

Santanu De was supported by a scholarship from All India Council for Technical Education.

International Journal of Numerical Methods for Heat & Fluid Flow
Vol. 19 No. 6, 2009
pp. 790-815

0961-5539
DOI 10.1108/09615530910973011

liquid-film drying devices (Alleborn *et al.*, 1999). Scientific interest in this type of flow began with the pioneering experimental works of Mills (1965) and Pan and Acrivos (1967), who provided the visualization of three-dimensional (3D) cavity flow with different aspect ratios (shown schematically in Figure 1). The classical problem of lid-driven cavity (LDC) has been studied extensively both experimentally (Aidun *et al.*, 1991; Koseff and Street, 1984a, b, c) and numerically (Ghia *et al.*, 1982; Schreiber and Keller, 1983; De Vahl Davis and Mallinson, 1976; Ku *et al.*, 1987; Iwatsu *et al.*, 1989; Chiang *et al.*, 1998). Owing to the simplicity of geometry, boundary conditions and complicated vortical structure, it has emerged as a reliable benchmark problem for the development of Navier–Stokes (NS) solvers (Babu and Korpela, 1994; Albensoeder and Kuhlmann, 2005). Recently, Shankar and Deshpande (2000) have comprehensively reviewed the LDC flow and identified crucial aspects open for investigations.

Many researchers (Ghia *et al.*, 1982; Schreiber and Keller, 1983) computed the steady two-dimensional (2D) flow driven by a moving top wall in a square cavity for a range of Reynolds numbers (the Reynolds number being defined as $\mathrm{Re} = U_{\mathrm{lid}}L/\nu$, where U_{lid} is the lid-velocity, L the cavity-width and ν the kinematic viscosity of the fluid enclosed). However, the 2D models provide only a first approximation since in experiments the cavity is limited in span by end walls, with important 3D effects induced by the no-slip conditions imposed thereon. Although, experimental measurements and visualizations across a cross-section validate the 2D solutions qualitatively, a quantitative comparison of velocity profiles fails. As pointed out in Koseff and Street (1984a), a major disagreement is seen in the size of downstream secondary eddy as a function of Reynolds number. The influence of 3D secondary circulation induced by the presence of rigid end-walls in finite-length cavities has been investigated by many researchers (Koseff and Street, 1984a, b, c; De Vahl Davis and Mallinson, 1976) Koseff and Street (1984a, b, c) demonstrated the inherent three-dimensionality of the LDC flow with the help of experiments using a square cross-section and various length-to-width aspect ratios $A = B/L$ (where B is the length of the cavity in spanwise direction), and with different Reynolds numbers based on the cavity-width. TGL vortices and corner vortices were observed apart from essential three-dimensionality and significant transverse motion. The above studies reveal that at very low Reynolds numbers, LDC flow remains almost 2D; it transforms to 3D flow with secondary vortices appearing in the spanwise plane at moderate Reynolds numbers. The flow bifurcates from a stationary one to a periodical one at a critical Reynolds number $\mathrm{Re} \sim O(10^3)$, with the onset of instability, which eventually leads to turbulence (Albensoeder *et al.*, 2001). However, the critical Reynolds number depends on length-to-width (A) and depth-to-width ($K = H/L$, where H is the depth of the cavity) aspect ratios. Transition to

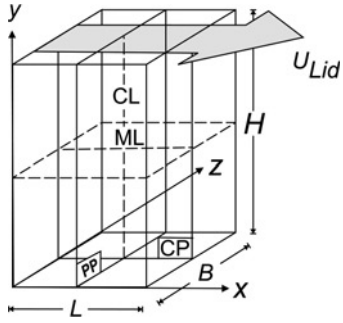

Figure 1.
A schematic showing the different planes and lines in a 3D lid-driven cavity

turbulence of LDC flow has been a major research topic since the pioneering work of Koseff and Street (1984a) and continues to be pursued even today (Leriche and Gavrilakis, 2000).

Experiments (Pan and Acrivos, 1967) and numerical simulations (Shen and Floryan, 1985; Gustafson and Halasi, 1985) on the 2D flow in a rectangular cavity have been carried out to investigate the structure and evolution of the vortices for different depth-to-width aspect ratios (K) and Reynolds numbers. Pan and Acrivos (1967) conducted experimental and numerical simulation on rectangular cavities of different aspect ratios $K = 0.5$-10 in order to study the flow structure when (Re, K) $\rightarrow \infty$. Shankar (1993) analyzed the Stokes' flow in a deep cavity and found that the primary vortex structure is related to the corner eddies. Numerical investigations of the physics of LDC flow in a deep cavity indicate the existence of critical aspect ratios at which the corner eddies merge together and form another primary eddy. There have been very few efforts (Albensoeder *et al.*, 2001; Cortes and Miller, 1994) to understand the 3D flow in deep cavities. Cortes and Miller (1994) made a comparative study of 3D and 2D cavity flows. Their numerical results show that, at moderate Reynolds numbers, the centerline velocity of a 3D cavity differs from that of a 2D cavity of the same aspect ratio. However, there is no work available in the literature for 3D flows in cavities with aspect ratio $K > 2$.

Lattice Boltzmann equation method (LBM), which is an alternative to solving NS equations is used here to simulate the flow inside the 3D cavity. LBM is based on microscopic kinetic equation for the particle distribution function. Unlike traditional numerical methods which solve the NS equations to obtain the macroscopic variables such as velocity and density, the LBM obtains these variables from the moment integrations of the particle distribution function. As such, the LBM has computational advantages, such as, simplicity of programming, intrinsic parallelism of the algorithm and data structure. Several standard, benchmark problems have been pursued by LBM and the results are shown to agree quite well with the corresponding NS solutions. Currently, a number of other complex flow problems are being simulated using the LBM approach (Huang *et al.*, 2005, 2006). The real superiority of the lattice Botlzmann method lies in the analysis of microscale flow and heat transfer problems. Recently, LBM has been extended to the flow in a microchannel (Agrawal *et al.*, 2005), where conventional solver fails. An introduction to the LBM theory, its methodology and the current status may be obtained from Chen and Doolen (1998), Qian *et al.* (1992), Succi (2001) and Yu *et al.* (2003). The single-relaxation-time (SRT) model (also known as Bhatnagar–Gross–Krook, or lattice BGK model) has been the most popularly employed one, owing to its simplicity. However, certain other models which offer a superior numerical stability than does the BGK model, have also been proposed. Among the latter, the multiple-relaxation-time (MRT) model (d'Humieres, 1992; Lallemand and Luo, 2000, 2003) and regularized LB (or RLB) model (Latt and Chopard, 2006) appear to be noteworthy. Considering the rapid pace with which the subject is developing, in the foreseeable future these alternative models (namely, MRT and RLB) are likely to play a significant role in the numerical prediction of flows. 2D lid-driven square cavity flow is a classical benchmark problem, with which SRT-LBM simulations have been extensively validated (Guo *et al.*, 2000, Chew *et al.*, 2002). 2D LDC flows with different aspect ratios (Cheng and Hung, 2006, Patil *et al.*, 2006) have also been simulated using SRT-LBM. Recently, diagonal-driven flow in 3D cavities has been studied using MRT-LBM technique by d'Humières *et al.* (2002) and it was found that MRT-LBM is superior

to SRT-LBM. This apart, there have been no efforts to investigate the vortex structure in 3D LDC flows in rectangular cavities using LBM.

In this work, we present the MRT-LBM simulation of flow inside a 3D LDC with different depth-to-width aspect ratios (K). The objectives of the present work are the following: (1) to study the influence of the aspect ratio and Reynolds number on the flow pattern in the 3D cavity, (2) to provide a comparison between present 3D results with previous 2D results and (3) to assess the performance of MRT-LBM in simulating internal 3D flows. For this purpose, the LBM approach is taken to model the 3D flow inside the cavity and the results are compared with benchmarked numerical solutions of NS equations. In this work, the currently practised MRT-LBM model has been implemented on the D3Q19 lattice. A parallel MRT-LBM code has been developed for numerical simulations.

The remainder of this article is organized as follows. In Section 2, the mathematical formulation of the MRT approach is described. In Section 3, results from MRT-LBM simulation of LDC flow in 3D cavity are presented and discussed. Finally, the major conclusions are summarized in Section 4.

2. Mathematical formulation

In this section, the MRT-LBM formulation is briefly presented. The original and a detailed description of the MRT methodology may be found in d'Humières *et al.* (2002).

2.1 Non-dimensionalization

Subsequently, dimensional quantities are identified by a prime, and reference quantities with the subscript "*ref*". In non-dimensional form, the individual quantities are

$$\mathbf{u} = \frac{\mathbf{u}'}{\Delta x'/\Delta t'}, \quad \mathbf{x} = \frac{\mathbf{x}'}{\Delta x'}, \quad t = \frac{t'}{\Delta t'}, \quad \nu = \frac{\nu'}{(\Delta x')^2/\Delta t'}, \quad U_{\text{lid}} = \frac{U'_{\text{lid}}}{\Delta x'/\Delta t'} \tag{1}$$

where $\Delta x' = x'_{ref}/(N_x - 1)$ is the lattice spacing, N_x being the number of lattice nodes placed within length x'_{ref} and $\Delta t'$ the timestep. Furthermore, U'_{lid} is the lid-velocity, $\mathbf{u}'$ the velocity and ν' the kinematic viscosity of the fluid. For the present flow configuration (see Figure 1), the cavity-width L' is chosen as the characteristic lengthscale x'_{ref}. Other physical variables are non-dimensionalized as follows:

$$\rho = \frac{\rho'}{\rho'_{ref}}, \quad f_\alpha = \frac{f'_\alpha}{\rho'_{ref}}. \tag{2}$$

In Equation (2), $\rho = \rho(\mathbf{x}, t)$ is the local mass density, and $f_\alpha = f(\mathbf{e}_\alpha, \mathbf{x}, t)$ is the local, instantaneous particle distribution function, which is a spatio-temporal function of discretized microscopic velocity space $\mathbf{e}_\alpha$. The Reynolds number characterizing this flow is given by

$$\text{Re} = \frac{U'_{\text{lid}} L'}{\nu'_{ref}} = \frac{U_{\text{lid}}(N_x - 1)}{\nu}. \tag{3}$$

Where ρ'_{ref} and ν'_{ref} are taken as density and kinematic viscosity of the fluid, respectively.

2.2 The lattice Boltzmann equation

The lattice Boltzmann equation, discretized in the velocity space but continuous in physical space and time, may be written as

$$\frac{\partial f_\alpha}{\partial t} + \mathbf{e}_\alpha \cdot \nabla f_\alpha = \Gamma_\alpha, \tag{4}$$

where Γ_α is the change in f_α due to inter-particle collisions. The discrete microscopic velocity is represented as

$$\{\mathbf{e}_\alpha \mid \alpha = 0, \ldots, (b-1)\} \tag{5}$$

where $\mathbf{e}_0 = 0$ refers to "resting" particles. With the discrete velocity set given, a set of b real numbers on each physical point $\mathbf{x}$ and at a time t,

$$\{f_\alpha(\mathbf{x}, t) \mid \alpha = 0, \ldots, (b-1)\} \tag{6}$$

is used to represent the particle distribution function at ($\mathbf{x}$, t) and discretized in velocity space. To obtain a numerical solution to Equation (4), two further discretizations are involved: those in the physical space and time. Suppose one considers a general case, where the time-evolution of Equation (4) is studied at each discrete physical location $\mathbf{x}_j$ on a discrete lattice space based on the set of b discrete velocities of Equation (5) according to a set of rules that enforces the local conservation laws. Then the fully discretized particle distribution function may be represented in a vector space $\mathbb{R}^b$ using the notation used in Lallemand and Luo (2000) as

$$|f_\alpha(\mathbf{x}_j, t_n)\rangle = \{f_0(\mathbf{x}_j, t_n), f_1(\mathbf{x}_j, t_n), \ldots, f_{(b-1)}(\mathbf{x}_j, t_n)\}^\top. \tag{7}$$

Here, f_α's are the distribution function of velocity $\mathbf{e}_\alpha$ at ($\mathbf{x}_j$, t_n).

The local and instantaneous macroscopic flow properties are related to the moments of the particle distribution functions in the following manner:

$$\rho(\mathbf{x}_j, t_n) = \sum_{\alpha=0}^{b-1} f_\alpha(\mathbf{x}_j, t_n) \quad \text{and} \quad \mathbf{j}(\mathbf{x}_j, t_n) = \rho\mathbf{u}(\mathbf{x}_j, t_n) = \sum_{\alpha=0}^{b-1} \mathbf{e}_\alpha f_\alpha(\mathbf{x}_j, t_n) \tag{8}$$

2.3 The MRT-LBM method

Given a chosen set of discrete velocities and corresponding distribution functions in the phase space $\mathbb{F} = \mathbb{R}^b$, an equal number of moments

$$|m_\alpha(\mathbf{x}_j, t_n)\rangle = \{m_0(\mathbf{x}_j, t_n), m_1(\mathbf{x}_j, t_n), \ldots, m_{(b-1)}(\mathbf{x}_j, t_n)\}^\top, \tag{9}$$

may be defined in the moment space $\mathbb{M} = \mathbb{R}^b$ of the distribution functions f_α. The mapping is linear and invertible, and is defined by

$$|m_\alpha\rangle = \mathsf{M}|f_\alpha\rangle, \quad |f_\alpha\rangle = \mathsf{M}^{-1}|m_\alpha\rangle, \tag{10}$$

where M is the linear transformation matrix. For a chosen velocity set $\{\mathbf{e}_\alpha\}$ (which is determined by the lattice-geometry), the transformation matrix M can be constructed

by applying the Gram–Schmidt orthogonalization procedure to monomials ($e^a_{\alpha,x}$ $e^b_{\alpha,y}$ $e^c_{\alpha,z}$) of cartesian components of the discrete velocities in 3D (Lallemand and Luo, 2003). The evolution equation (4) of the MRT-LBM can be written in discretized form as

$$|f_\alpha(\mathbf{x}_j + \mathbf{e}_\alpha, t_n + 1)\rangle - |f_\alpha(\mathbf{x}_j, t_n)\rangle = -\mathsf{M}^{-1}\hat{\mathsf{S}}\Big[|m_\alpha(\mathbf{x}_j, t_n)\rangle - |m^{(eq)}_\alpha(\mathbf{x}_j, t_n)\rangle\Big]. \quad (11)$$

In Equation (11), the collision matrix $\hat{\mathsf{S}} = \mathsf{MSM}^{-1}$ is diagonal, whose elements $s_\alpha = \{s_0, s_1, \ldots, s_{b-1}\}$ are the rates with which each element of $|m_\alpha\rangle$ relaxes towards the respective equilibrium value $|m^{(\mathrm{eq})}_\alpha\rangle$. The numerical values of relaxation rates $\{s_\alpha\}$ are determined by a linear analysis to obtain an optimal numerical stability (Lallemand and Luo, 2000). The b moments can be divided into two groups: hydrodynamic (conserved) moments and the kinetic (non-conserved) moments. Hydrodynamic moments are conserved locally during the collision process, so that $m^{(\mathrm{eq})}_\alpha = m_\alpha$, whereas the kinetic moments are not conserved during the collision process so that $m^{(\mathrm{eq})}_\alpha \neq m_\alpha$ (d'Humières *et al.*, 2002). For models designed to simulate athermal fluids, mass density (ρ), momentum ($\mathbf{j}$) are the only hydrodynamic moments. On the other hand, equilibrium values of kinetic moments are functions of ρ and $|\mathbf{j}|^2$ for scalars, and $\mathbf{j}$ times certain functions of ρ and $|\mathbf{j}|^2$ for vectors, and so on.

It may be noted that the SRT-LBM model is a special case of its MRT-LBM counterpart: by choosing a special set of parameter values in the equilibria of the moments $m^{(\mathrm{eq})}_\alpha$, and a single relaxation rate $s_\alpha = \tau^{-1}$, the MRT-LBM model reduces to the SRT-LBM model. In the MRT framework, all modes (i.e. moments) are orthogonal and their relaxation rates can be controlled individually. This allows the MRT model to include the maximum number of adjustable parameters, and hence achieve superiority over the SRT-LBM.

2.4 The D3Q19 lattice

A schematic of the D3Q19 lattice (d'Humières *et al.*, 2002) is shown in Figure 2. For this lattice, the discrete velocity set is

$$\mathbf{e}_\alpha = \begin{cases} (0,0,0), & & & \alpha = 0 \\ (\pm1,0,0), & (0,\pm1,0), & (0,0,\pm1), & \alpha = 1,2,\ldots,6 \\ (\pm1,\pm1,0), & (\pm1,0,\pm1), & (0,\pm1,\pm1), & \alpha = 7,8,\ldots,18 \end{cases} \quad (12)$$

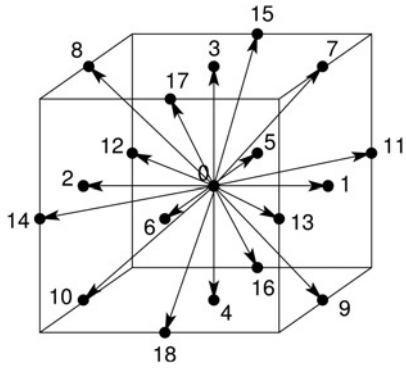

Figure 2.
Structure of the lattice unit cell in D3Q19 model for MRT

In the present work, the transformation matrix M, corresponding moments m_α, their equilibrium values $m_\alpha^{(\mathrm{eq})}$, and the collision matrix $\hat{\mathbf{S}}$, are taken exactly as suggested by d'Humières *et al.* (2002).

2.5 Boundary and initial conditions

Following the literature (Shankar and Deshpande, 2000) for the cubic cavity problem, Dirichlet boundary conditions are imposed on the walls:

$$\left.\begin{array}{ll} \text{Left and right walls:} & u = v = w = 0 \ \text{ at } x = (0, N_x) \\ \text{Front and rear walls:} & u = v = w = 0 \ \text{ at } z = (0, N_z) \\ \text{Bottom wall:} & u = v = w = 0 \ \text{ at } y = 0 \\ \text{Top wall:} & u = U_{\mathrm{lid}}, \ v = w = 0 \ \text{ at } y = N_y \end{array}\right\} \tag{13}$$

For laminar flow regimes (far from instability or transition to turbulence), we may expect the flow-field to be symmetric about the center plane CP (Iwatsu *et al.* (1989) reported that the flow remains symmetric until very high Reynolds numbers, Re < 3,000). Taking advantage of this feature, symmetry conditions are imposed at $z = N_z/2$, and only one-half of the cavity ($0 < z \leq N_z/2$) is taken as the computational domain. The corresponding symmetry conditions are

$$\frac{\partial \mathbf{u}}{\partial z} = 0 \ \text{ on } \ (x, y, N_z/2) \tag{14}$$

(a few runs including the full domain revealed that the results remain identical to those with symmetry conditions). These physical boundary conditions may be implemented within the LBM code in different ways. The actual method of implementation in the present code is discussed briefly in the following subsections.

2.5.1 Stationary-wall conditions. In earlier attempts for 3D LDC flow simulation d'Humières *et al.* (2002) used "bounce-back" condition on all the stationary walls. It was found that the bounce-back condition is only first order accurate (Ziegler, 1993; Ginzbourg and Adler, 1994). This degrades the LBM, since numerical accuracy of Equation (11) for the interior mesh points is second order. On the five stationary walls the "link-bounce-back" condition is applied which has been claimed to be second-order accurate (Ziegler, 1993). He *et al.* (1997) confirmed this result by analyzing the slip velocity near the wall node for Poiseuille flow. For the implementation of the boundary condition, herein the mesh points nearest to the wall are placed at a distance equal to one-half of the mesh size from the wall.

2.5.2 Moving-wall conditions. For the moving lid, we have used the link-bounce-back condition in a slightly modified form as proposed by Bouzidi *et al.* (2001). This boundary condition is obtained in the velocity space by assigning particle distributions to

$$f_{\bar{\alpha}} = f_\alpha + 2\omega_\alpha \rho_0 \frac{\mathbf{e}_{\bar{\alpha}} \cdot \mathbf{U}_{\mathrm{lid}}}{c_s^2} = f_\alpha - 2\omega_\alpha \rho_0 \frac{\mathbf{e}_\alpha \cdot \mathbf{U}_{\mathrm{lid}}}{c_s^2} \tag{15}$$

where $\omega_0 = 1/3$, $\omega_\alpha = 1/18$ for $\alpha \in \{1, \ldots, 6\}$ and $\omega_\alpha = 1/36$ for $\alpha \in \{7, \ldots, 18\}$. ρ_0 is the initial density and $f_{\bar{\alpha}}$ represents distribution function of $\mathbf{e}_{\bar{\alpha}} = -\mathbf{e}_\alpha$. In the present method, the boundary condition (Equation (13)) is implemented such that the particle distribution that is being streamed to the moving lid is reflected back to its original position with an addition of momentum due to the moving lid.

2.5.3 Symmetry conditions. On the plane CP (x, y, $N_z/2$), flow-symmetry is imposed as described in Lu *et al.* (2002).

2.5.4 Initial conditions. At the time of starting the simulations ($t = 0$), the fluid-velocities at all the nodes $\mathbf{u}(\mathbf{x}, 0)$ are initialized to zero. The initial density $\rho(\mathbf{x}, 0)$ is set to a value of 1.0 (d'Humières *et al.*, 2002). The initial equilibrium distribution function $f_\alpha^{(eq)}(\mathbf{x}, 0)$ is then evaluated corresponding to these conditions. The initial distribution function is taken as the corresponding equilibrium values, $f_\alpha(\mathbf{x}, 0) = f_\alpha^{(eq)}(\mathbf{x}, 0)$.

2.6 Numerical code

The MRT-LBM equation (11) is solved on a uniform 3D mesh along with boundary and initial conditions described in the previous section. Each numerical timestep consists of three different steps:

(1) collision;

(2) streaming; and

(3) boundary condition steps

as is usually followed in the LBM approach. Computations were carried out with a parallel code, originally developed by the authors using MPI technique and written in the C++ programming language. The code has been tested to run on both a PC-cluster as well as on a IBM-Regatta parallel computing system.

Shown in Figure 3 is the variation of the CPU time required (per lattice node per timestep) by the PC-cluster as a function of the number of processors employed. It may be seen from this figure that the CPU time decreases almost linearly with increase in the number of processors. This further indicates that the time spent in data-transfer between the processors is negligible compared to the time taken for computing, over the range of problem-size and number of processors employed in these studies. This demonstrates an efficient parallelization of the code, as well as the suitability of LBM technique for parallel computing.

3. Results and discussion

In this section, we discuss the numerical grids used for the different simulations, grid independence study, validation of the present numerical code, the results obtained for 3D rectangular cavities with various aspect ratios and Reynolds numbers.

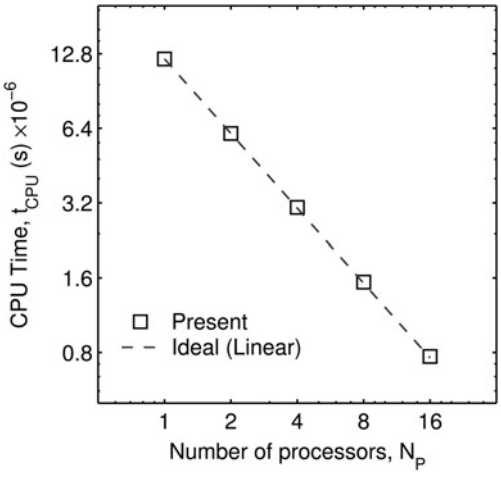

Figure 3.
Variation of the computing time taken per timestep per lattice node as a function of total number of processors employed

3.1 Grid systems, convergence and grid-independence study

LBM belongs to a class of solvers analogous to the pseudo-compressible solvers employed for incompressible NS equations. In order to correctly simulate incompressible flow one has to ensure that Mach number, $\mathrm{Ma} = U_{\mathrm{lid}}/c_s \ll 1$. In the present simulations, $\mathrm{Ma} < 0.15$ is chosen, and hence, c_s being a constant (=1), the velocity U_{lid} must be small enough. A lid-velocity of $U_{\mathrm{lid}} = 0.1$ is prescribed in all the simulations. Therefore, to simulate flows of high Reynolds numbers (see Equation (3)), one has to employ a large number of lattice nodes, where the dimensionless viscosity ν is sufficiently large but lies within the numerical stability limit (in the LBGK setting, $\nu \leq 0.5$).

Table I presents the typical number of lattice points used in the present simulations. The number of lattice points (N_x, N_y, N_z) used in each direction vary with the aspect ratio (K) and the Reynolds number. In these simulations, the aspect ratio $A = 1$ is chosen. The simulations were considered to have reached a steady-state when the difference in the local velocity values (1,000 timesteps apart) reduces to less than 1 per cent of the local velocity over the entire flow-field.

Presented in Table II is the grid independence of the results established for the present 3D LDC simulations at $\mathrm{Re} = 1{,}000$ and $K = 1$. Here, the results obtained on two different grids are summarized in terms of the minimum of the x-directional velocity component along the line CL. It is observed that the results obtained with the two grid-systems differ within about 0.5 per cent, and hence may be accepted as grid-independent. However, it is to be noted that the computational requirement becomes prohibitively huge for higher aspect ratios (e.g. $K = 4$), if one intends to use the same number of grid points comparable to corresponding 2D simulations. Therefore, our simulations for $K = 4$ are restricted to a grid resolution of ($129 \times 513 \times 129$), which was the practical limit imposed by the available computing resources. This is not claimed to be grid-independent, but the computed vorticity magnitudes were within 5-6 per cent from the corresponding results with ($97 \times 513 \times 97$) lattice nodes.

Table I.
Typical number of lattice points used in the present 3D LDC simulations ($A = 1$)

	$K=0.25$			$K=0.5$			$K=1$			$K=2$			$K=4$		
Re	N_x	N_y	N_z	N_x	N_y	N_z	N_x	N_y	N_z	N_x	N_y	N_z	N_x	N_y	N_z
0.01	97	25	97	73	37	73	33	33	33	33	65	33	33	129	33
100	97	25	97	73	37	73	33	33	33	33	65	33	33	129	33
400	145	37	145	97	49	97	65	65	65	65	129	65	65	257	65
1,000	193	49	193	129	65	129	97	97	97	97	193	97	129	513	129

Table II.
Grid-dependence study for ($K = A = 1$, $\mathrm{Re} = 1{,}000$)

	Mesh		
	($97 \times 97 \times 97$)	($129 \times 129 \times 129$)	% change
$u_{\min}$	−0.282536004	−0.282606638	0.025
$y_{\min}$	0.132654061	0.132640796	0.010

Note: Here $u_{\min}$ indicates the minimum velocity in the x direction along the line CL, and $y_{\min}$ represents the location where $u_{\min}$ occurs

3.2 Validation of numerical code

In this subsection, first we present a comparison of the steady-state velocity profile obtained from the present MRT-LBM simulations with the NS solutions published in the literature. These cases correspond to a lid-driven flow in a cubic cavity ($A = K = 1$) as well as in a rectangular cavity ($A = 1, K = 2$ and $A = 2, K = 1$) at different Reynolds numbers.

Shown in Figure 4 are the normalized x- and y-components of velocity profiles along the vertical (CL) and horizontal (ML) centerline at the plane CP, respectively (these correspond to, CL: ($N_x/2$, y, $N_z/2$), ML: (x, $N_y/2$, $N_z/2$) and CP: (x, y, $N_z/2$), see Figure 1). Solid lines represent the results obtained from the present simulations, whereas the discrete points denote the 3D pseudo-spectral solution of NS equations by Albensoeder and Kuhlmann (2005). It is seen that the comparison is excellent at all Reynolds numbers considered here.

Shown in Figure 5 are the normalized x-components of velocity profiles along the vertical (CL) centerline at the plane CP for a cavity of aspect ratio $K = 2$. Solid lines represent the results obtained in the present simulations, whereas the discrete points denote the 3D NS results by Albensoeder and Kuhlmann (2005). It is seen that the present MRT-LBM simulations agree well with the NS results of Albensoeder and Kuhlmann (2005) at all Reynolds numbers for the deep cavity also. A further validation was attempted by carrying out the flow simulation using a well-established, commercial CFD package, ANSYS-CFX. This employs a second-order accurate, combined finite difference/finite volume technique for solution of NS equations. The number of grid-points employed in the ANSYS-CFX simulations were identical to that used in our LBM simulations. The results from ANSYS-CFX also compare excellently with the present MRT-LBM results at Re = 1,000.

The LBM-technique is claimed to offer a second-order accuracy in time. This aspect was examined by a comparison of the time-evolution of velocities against the predictions by the NS computations (Albensoeder and Kuhlmann, 2005). Shown in Figure 6 is such a comparison of the time-evolution of v-velocities at two physical locations namely, (0.90908, 0.5, 1) and (0.22223, 0.5, 1). The initial flow-field was taken as zero-velocities at all locations, which is also the case with the computations by Albensoeder and Kuhlmann (2005). In the present simulations, ($97 \times 97 \times 193$) lattice nodes were employed whereas Albensoeder and Kuhlmann (2005) employed ($32 \times 32 \times 32$) grids. The present LBM predictions closely agree with the NS solution

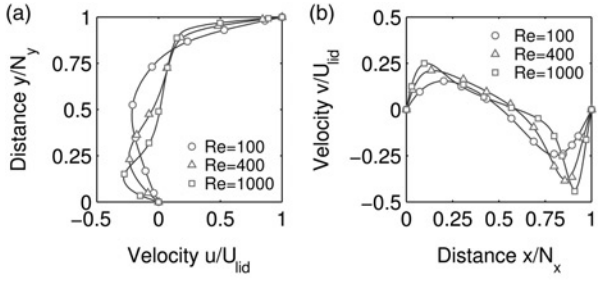

Notes: Plots of (a) $u(0.5, y, 0.5)$, and (b) $v(x, 0.5, 0.5)$. Lines: present LBM results, symbols: results from Albensoeder and Kuhlmann (2005) for Re = 100, 400, and 1,000 ($K = A = 1$ for all cases)

Figure 4.
Comparison of velocity profiles on the CP-plane for a cubic cavity

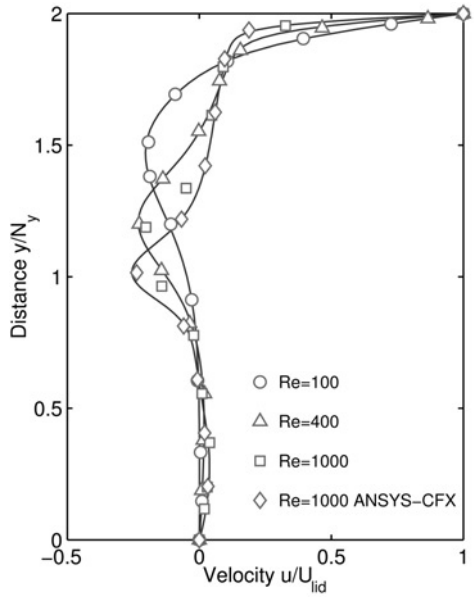

Figure 5.
Comparison of velocity profiles on the CP-plane for a cavity of ($K = 2$, $A = 1$). Plots of $u(0.5, y, 0.5)$

Notes: Lines: present LBM results; the symbols "○, △, □" represent results from Albensoeder and Kuhlmann (2005) for Re = 100, 400 and 1,000 respectively. The symbols '◇' are results from ANSYS-CFX

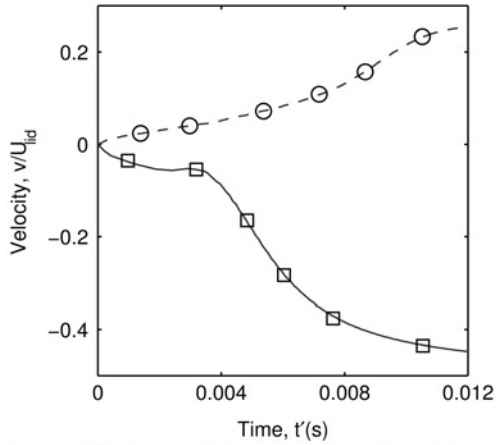

Figure 6.
Time-evolution of velocities for the case ($K = 1$, $A = 2$, Re = 1,000)

Notes: Validation of the present results with spectral NS computations. Lines: present,symbols: from Albensoeder and Kuhlmann (2005). Solidline: v-velocity at (0.90908,0.5, 1). Dashed line: v-velocity at (0.22223, 0.5, 1)

results. Hence it is concluded that the LBM method offers a technique for accurate simulation of time-dependent flow problems also.

3.3 Results for the 3D rectangular cavity

In this subsection, results of both shallow ($K < 1$) and deep ($K > 1$) cavity simulations are presented along with those of cubic ($K = 1$) cavity. In all the cases, a spanwise aspect ratio of $A = 1$ is chosen. Figure 7 represents the steady-state velocity profile along line CL for different aspect ratios ($K = 0.25$, 0.5, 2,4) and Reynolds numbers (Re = 0.01, 100, 400, 1,000). It may be observed that for shallow cavities (Figures 7(a) and (b)) the region close to the bottom wall shows a significant boundary layer, whereas for high aspect ratios, it is absent. Furthermore, from Figure 7(a) it is seen that a flow-reversal occurs near the bottom wall, as the Reynolds number is increased from 100 to 400. Subsequently, we shall return to a discussion on this aspect.

Cheng and Hung (2006) presented the drag coefficient on the lid for a 2D rectangular cavity flow for different sets of ($K < 1$, Re). They reported that the drag coefficient decreases significantly as either K or Re increases. In order to assess the difference between 2D and 3D results, we calculated the average drag coefficient from the present simulations. Here the drag coefficient is defined as

$$C_f = \frac{2F}{\rho\, U_{\text{lid}}^2 L} \tag{16}$$

where F is the net drag force on the lid, which in turn is defined as

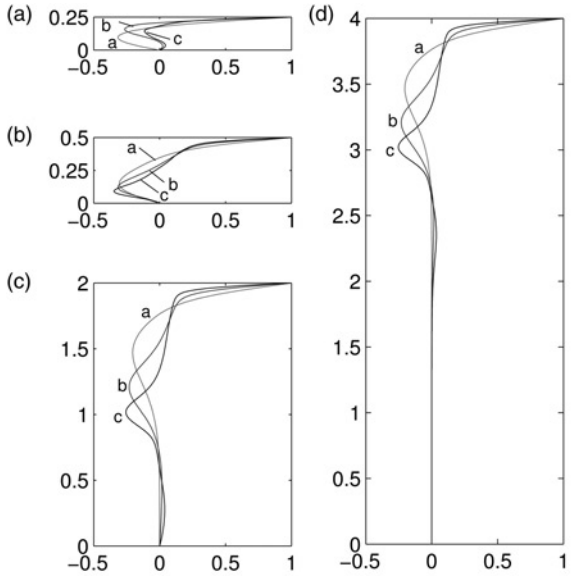

Notes: Following notations are used for Reynolds number: "a" for Re = 100, "b" for Re = 400,and, "c" for Re = 1,000 ($A = 1$ for all cases)

Figure 7.
Plots of x-component of velocity (u) along CL with different aspect ratios, $K =$ (a) 0.25, (b) 0.5, (c) 2.0, and, (d) 4.0 at different Re

$$F = \int \mu \frac{\partial u}{\partial y} \, dS, \tag{17}$$

the integration being carried out over the entire wetted area of the lid. In order to compare the present 3D and reported 2D results, we have also calculated the drag coefficient along the line $z = N_z/2$ on the lid-surface. Shown in Table III are the drag coefficients for shallow and cubic cavities at different Reynolds numbers. It is observed that the drag coefficient calculated from 2D simulations deviates the maximum (33 per cent) for shallow cavity ($K = 0.25$, Re $= 100$) from an equivalent 3D simulation. This deviation decreases as the aspect ratio is increased up to $K = 1$.

The drag coefficient was also calculated for cavities of aspect ratio greater than 1. It was observed that beyond $K = 1$, the calculated C_f values did not change much with the aspect ratio ($K = 2$ or 4) for a particular Reynolds number (not included in Table III).

The 3D flow structure in the plane CP (see Figure 1) was investigated for various aspect ratios and Reynolds numbers. In the following discussions, we first present the results of shallow cavities, and subsequently, of the cubic and deep cavities.

3.3.1 Shallow cavities ($K < 1$). Figure 8 shows the velocity vectors and vorticity contours for the shallow cavity ($K = 0.25$) flow at different Reynolds numbers, (Re $= 0.01$, 100, 400, 1000). The effect of Reynolds number on the vortex structure in the cavity is clearly seen. In the limit of creeping flow (Re $= 0.01$), the flow structure is characterized by a single, large, primary eddy (Figure 8(a)); secondary eddies at the bottom corners were not prominently observed. The vorticity contours are quite symmetric about the vertical centerline (CL). The center of the primary eddy is located at the middle the cavity, but slightly towards the moving lid.

As Re is increased from 0.01 to Re $= 1{,}000$, the center of the primary eddy is found to shift towards the downstream sidewall of the cavity, and the flow pattern no longer remains symmetric about the vertical centerline due to the increasing domination of inertia force. A similar trend has been reported from 2D simulations also (Cheng and Hung, 2006). The velocity vectors and vorticity contour-plots reveal that the strength of the primary vortex decreases with increasing Re (Figure 8).

At Re $= 1{,}000$ (Figure 8(d)), a second primary vortex appears adjacent to the first primary vortex. The second primary vortex is found to have an opposite direction (counter-clockwise here), and a lower strength compared to the first primary vortex.

K	Re $= 0.01$	Re $= 100$	Re $= 400$	Re $= 1{,}000$
0.25[a]	5,390	0.5293	0.1986	0.1112
0.25[b]	4,975	0.5089	0.1914	0.0983
0.25[c]	3,346	0.3369	–	0.04298
0.50[a]	3,755	0.4036	0.1436	0.0743
0.50[b]	3,388	0.3801	0.1389	0.0668
0.50[c]	2,845	0.2926	–	0.0424
1.00[a]	2,839	0.2724	0.1074	0.0603
1.00[b]	2,621	0.2586	0.1034	0.0586
1.00[c]	2,764	0.2874	–	0.04201

Table III.
The average drag coefficients (C_f) on the moving wall at different aspect ratios (K) and Reynolds numbers Re (for all cases, $A = 1$)

Notes: [a]Present results, average drag coefficient calculated over entire lid surface; [b]present results, average drag coefficient calculated at $z = 0.5$ on lid surface; [c]2D results reported by Cheng and Hung (2006)

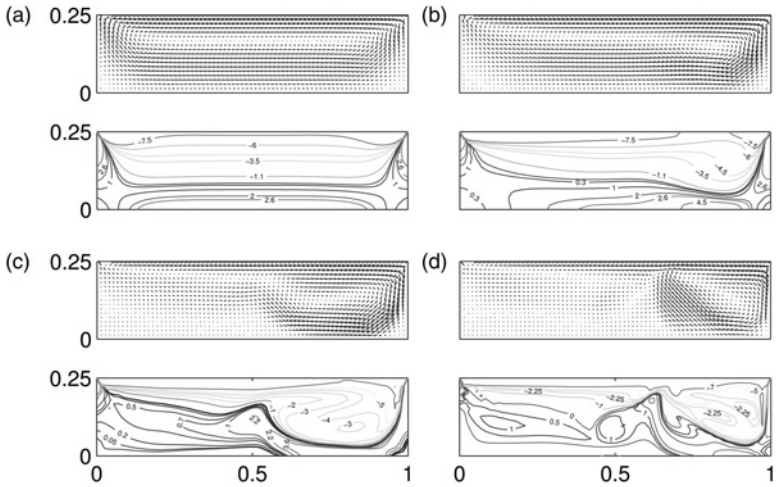

Notes: Aspect ratios $K = 0.25$, $A = 1$; the abscissa and ordinate correspond to distances x/N_x, y/N_y across the plane CP. Reynolds numbers correspond to: (a) 0.01, (b) 100, (c) 400, and (d) 1,000, respectively. Velocity components are in the plane of the paper (CP) whereas vorticity component is normal to the paper; other components are not shown

Figure 8.
Velocity vector (top row) and vorticity contour (bottom row) plot

Furthermore, the size of second primary vortex is smaller than the first primary vortex. This implies that as the Reynolds number is increased, the flow structure within the cavity becomes increasingly more complex.

The velocity vectors and vorticity contours at $K = 0.5$ are shown in Figure 9. The vortex structure remains almost similar when $\mathrm{Re} \leq 100$. When $\mathrm{Re} > 100$, however, the size of the upstream bottom corner vortex increases remarkably with increasing Re while the primary vortex starts shrinking in size (Figures 9(b)-(d)). Another important difference from $K = 0.25$ case is that the primary vortex becomes more circular when $K = 0.5$. This trend continues as the aspect ratio increases.

3.3.2 Cubic cavity ($A = K = 1$). Shown in Figure 10 are the velocity vectors and vorticity contours for a cubic cavity ($A = K = 1$). At low Reynolds numbers, Figures 10(a) and (b), the region occupied by the primary vortex is relatively small, due to the highly diffusive transport of the vorticity, and the boundary layers near the walls are considerably thick. On the other hand, at high Reynolds numbers, Figures 10(c) and (d), the primary vortex grows in size and occupies most of the central region of the cavity cross-section; the boundary layer is seen to be limited to very thin regions near the walls. In this case, the vorticity transport is dominated by the advection created due to motion of the top lid.

Furthermore, a pair of small, secondary vortices appear near the bottom corners of the cavity. These secondary vortices are not evident in Figures 10(a) and (d), because of the relatively small magnitude of the velocities in these regions compared to that in the central region of the cavity. However, a plot of streamlines (not shown here) revealed such secondary vortices at all Reynolds numbers. These secondary eddies have been well characterized by previous 2D simulations (see e.g. Ghia *et al.*, 1982; Patil, *et al.*, 2006). For instance, Ghia *et al.* (1982) calculated the vorticity at the center of the

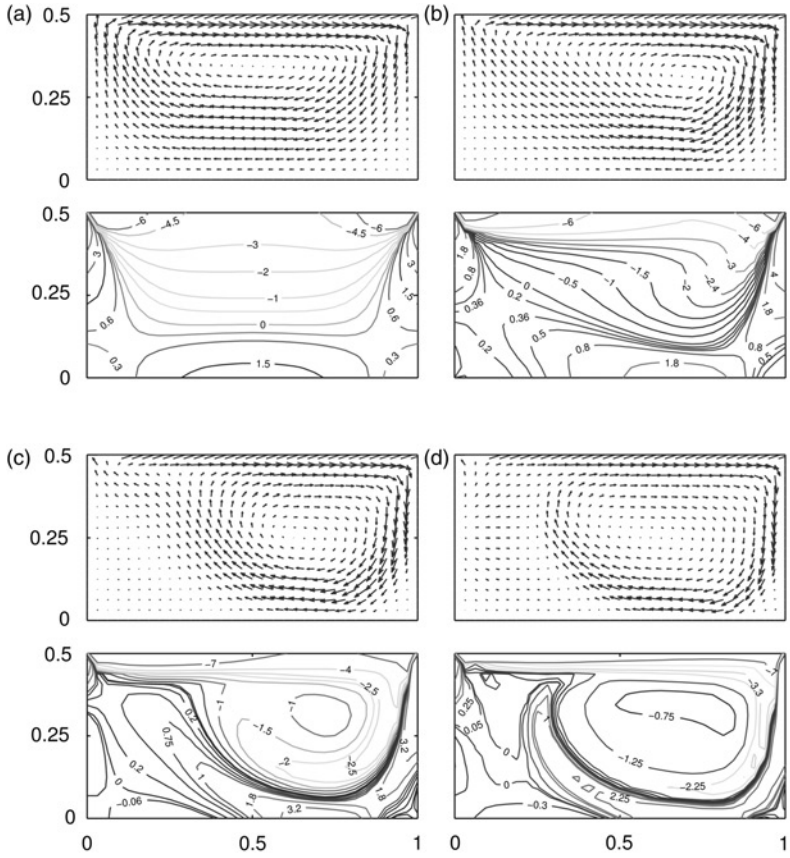

Notes: Aspect ratios $K = 0.5$, $A = 1$; The abscissa and ordinate are same as in Figure8. Reynolds numbers correspond to: (a) 0.01, (b) 100, (c) 400 and (d) 1,000, respectively. Velocity and vorticity components same as in Figure 8

Figure 9.
Velocity vector (top row) and vorticity contour (bottom row) plot

downstream secondary eddy as $\Omega_z = 0.4335$ for a square cavity at Re = 400. Our present simulations yield a value of $\Omega_z = 0.3545$.

As Re is increased, the center of the primary vortex (x_c, y_c) shifts towards the downstream wall, and simultaneously it moves down towards the bottom wall of the cavity (see Figures 10(a)-(d)). In 2D simulations, the center of the primary vortex has been observed to shift towards the downstream side of the cavity until the Reynolds number increases to about 100, but there onwards it asymptotically moves towards the geometric center of the cavity (Ghia *et al.*, 1982) with further increase in Reynolds number. The variation of (x_c, y_c) with Re has been the most widely investigated characteristic of the lid-driven cavity flow in 2D simulations. Therefore, we have also examined this aspect in our study. Shown in Figure 11 is the computed location of the primary eddy at different Reynolds numbers, which clearly shows the movement of location (x_c, y_c) with Re. Also shown are the results from NS simulations using 2D (Ghia *et al.*, 1982; Cheng and Hung, 2006) and 3D (Iwatsu *et al.*, 1989) flow models. Shankar (1993) obtained the theoretical result in the 2D creeping flow limit (Re $\rightarrow 0$), as

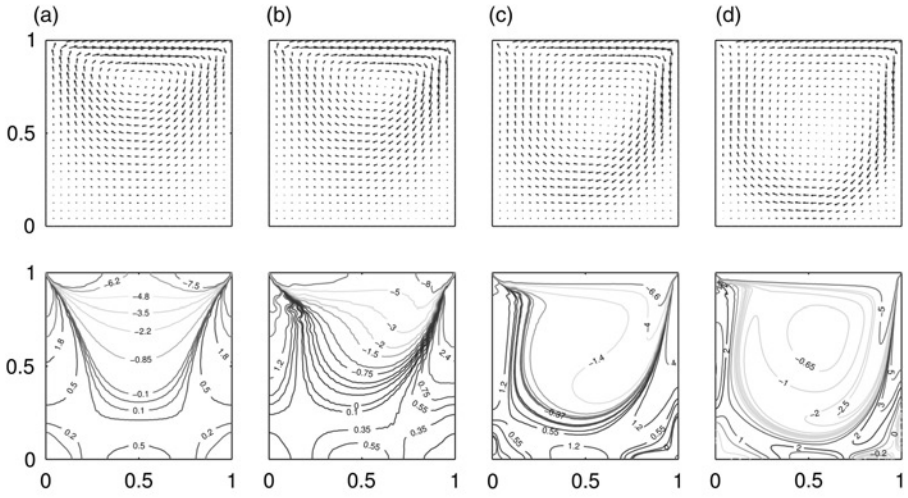

Notes: Aspectratios $A = K = 1$; the abscissa and ordinate are same as in Figure 8. Reynolds numbers correspond to: (a) 0.01, (b) 100, (c) 400 and (d) 1,000, respectively. Velocity and vorticity components same as in Figure 8

Figure 10.
Velocity vector (top row) and vorticity contour (bottom row) plot

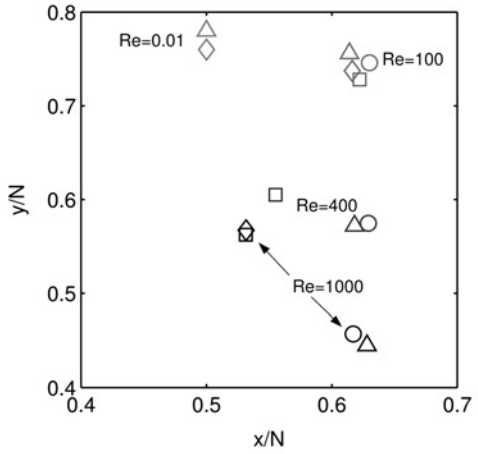

Notes: Present results (△) are plotted against different 2D and 3D results. The symbols "○, □, ◇" represent the 3D results of Iwatsu *et al.* (1989), 2D results of Ghia *et al.* (1982) and Cheng and Hung (2006) respectively

Figure 11.
Center of the primary vortex at CP for a cubic cavity ($A = K = 1$)

($x_c = 0.5, y_c = 0.76$). It may be observed from Figure 11 that the results of 2D- and 3D-simulations agree very well for Re = 0.01 and Re = 100. However, for Re = 400 and Re = 1,000, the predicted locations (x_c, y_c) from 2D and 3D flow models are significantly different. We believe that this difference is because of an enhanced motion in the transverse direction.

Shown in Table IV are the present results of (x_c, y_c) and the vorticity at that location, Ω_c for different Reynolds numbers. In order to make a quantitative comparison, the results reported by previous workers using 2D (Ghia *et al.*, 1982; Cheng and Hung, 2006) and 3D (Iwatsu *et al.*, 1989) NS simulations, as well as 3D NS simulations using ANSYS-CFX are also included here. It may be noted that the present MRT-LBM predicts a comparable value of Ω_c for the low Reynolds number case (Re = 0.01), whereas it predicts a much lower Ω_c for higher Reynolds number cases (Re $\geq$ 100). This may be attributed to the presence of boundary layers near the transverse side-walls.

A further comparison of results from 3D flow-model against those from 2D flow-model is shown in Figure 12. Here, the u, v-velocity profiles along the lines ($N_x/2$, y, $N_z/2$) and (x, $N_y/2$, $N_z/2$), respectively are plotted, at two Reynolds numbers. Very close to the walls, the velocity profiles predicted by the two models are almost identical. Further, it may be observed that at Re = 100, the velocity profiles deviate a little whereas at higher value, namely, Re = 1,000, the velocity profiles predicted by 3D computations are significantly different in comparison to those of 2D computations. This could be attributed to the development of a strong secondary flow (particularly at regions away from the walls) at high Reynolds numbers. We shall subsequently return to this issue.

Shown in Table V, are the horizontal (x_D) and vertical (y_D) distances which characterize the size of the downstream-secondary eddy. Included in this table are the results of numerical simulations (2D by Ghia *et al.*, 1982 and 3D by Iwatsu *et al.*, 1989) and experimental measurements ($A = 1$ by Pan and Acrivos, 1967) and $A = 3$ by Koseff and Street, 1984a). To compare the results reported by Pan and Acrivos (1967), the flow in a cubic cavity ($K = 1$) has been studied at Re = 500 (the results are shown in Table V). The 3D simulations (both Iwatsu *et al.* (1989) and the present) are seen to predict y_D closer to the experimental data than the corresponding 2D simulations. However, the minor difference with the results at Re = 1,000 reported by Koseff and Street (1984a) may be attributed to the weakened 3D effects as they have used a spanwise wider cavity.

3.3.3 Deep cavities ($K > 1$). Shown in Figures 13 and 14 are the velocity vectors and vorticity contours for cavities with $K = 2$ and $K = 4$, respectively.

It is noticed that a series of counter-rotating primary vortices, of successively weaker vorticity magnitudes, are formed below the moving lid. For the case of $K = 2$, two such primary vortices and for $K = 4$, three primary vortices are observed. It is seen from the velocity vector plots that, as the Reynolds number increases, the center of the first primary vortex moves downwards with respect to the top lid. This feature has been reported in the case of flow in 2D deep cavities also (Patil *et al.*, 2006). It is further observed from Figures 13(a) and (b), that the velocity near the bottom wall region reduces to very small values. For a given cavity depth $K > 1$, there exists a critical Reynolds number below which the regions close to the bottom wall may be approximated by the limiting case of creeping flow. In such cases, the flow structure near the bottom wall is symmetric about the line CL (Pan and Acrivos, 1967; Patil *et al.*, 2006). Above this critical Reynolds number, the flow near the bottom wall loses symmetry about the line CL. This is seen from the results shown in Figures 13(c) and (d). However, when the aspect ratio is increased, the flow symmetry near the bottom wall region is regained, as may be seen from Figures 14(c) and (d). Therefore, for an infinitely deep cavity with very high Reynolds number limiting case of creeping flow may be approached near the bottom wall of the cavity. Since the flow velocity becomes very small near the bottom wall region, the velocity vector plots in Figures 13 and 14

	Re = 0.01		Re = 100		Re = 400		Re = 1,000	
	(x_c, y_c)	Ω_c	(x_c, y_c)	Ω_c	(x_c, y_c)	Ω_c	(x_c, y_c)	Ω_c
Cheng and Hung (2006)	(0.5, 0.2348)	3.2211	(0.6162, 0.2628)	3.1703	–	–	(0.5315, 0.4328)	2.0500
Ghia *et al.* (1982)	–	–	(0.6220, 0.2720)	3.1665	(0.5547, 0.3950)	2.2947	(0.5313, 0.4375)	2.0497
Iwatsu *et al.* (1989)	–	–	(0.6292, 0.2541)	–	(0.6298, 0.4253)	–	(0.617, 0.543)	–
ANSYS-CFX	(0.5, 0.221)	3.3356	(0.623, 0.249)	2.8864	(0.625, 0.422)	1.3722	(0.593, 0.539)	0.6687
Present	(0.5, 0.220)	3.3743	(0.614, 0.244)	2.9213	(0.618, 0.428)	1.4043	(0.591, 0.543)	0.6811

Notes: ANSYS-CFX results correspond to 3D. Here y_c is measured from the moving lid and Ω_c is the z-component of vorticity at (x_c, y_c)

Table IV.
Comparison of results for cubic cavity ($K = A = 1$) at different Reynolds numbers: location of the center of primary vortex, and vorticity at that point are compared with previous 2D/3D results

are not able to reveal this feature. However the vorticity plots in Figures 13 and 14 exhibit a symmetry near the bottom wall.

In Table VI, we have summarized the results of simulations for aspect ratios $K \geq 1$ and Reynolds numbers. Shown here are the location and vorticity at the center of the primary vortices. It may be seen, for the deep cavity flow, the sizes and center position of the large vortices near the top lid appear to be strongly affected by Re, but is not so much by the cavity-aspect ratio. Furthermore, for $K = 4$ and all Reynolds numbers, the center of the third primary eddy approaches the mid-plane ($x_c \approx 0.5$) which is the result for creeping flow limit. The vertical distance between two successive primary eddies is found to be 1.646 (between first and second) and 1.63 (between second and third) for Re = 0.01. In comparison, the 2D theoretical solution (Shankar and Deshpande, 2000) for the limiting case of infinitely deep cavity and Stokes flow ($K \to \infty$, Re $\to 0$) is 1.396. An examination of the data from 2D simulations provided in Cheng and Hung (2006) corroborates this. Hence, we may conclude that the 3D simulations lead to a result wherein the adjacent primary eddies are slightly placed farther apart (about 17 per cent) in the vertical direction, in comparison to the 2D results.

3.3.4 Secondary Flow. The structure of the *secondary flow* for different aspect ratios and Reynolds numbers is presented in this section. Shown in Figures 15 and 16 are the velocity vectors in the perpendicular plane (PP) for $K = 0.5$ and $K = 1$, respectively.

It is seen at low Reynolds number that the flow in shallow cavities remains almost parallel to the cavity side-walls. At Re = 400, a pair of corner vortices are formed adjacent to the top wall of the cavity (Figure 15(a)). Flow-streamlines at the plane PP no longer remain parallel. At Re = 1,000, the flow-field becomes very complex, with a pair

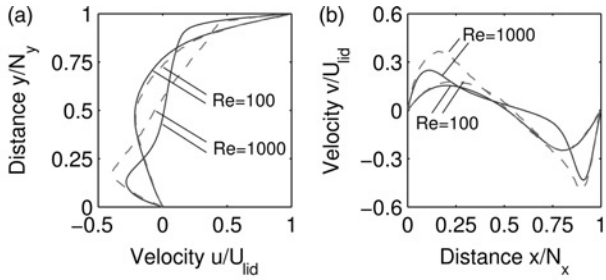

Notes: Solid lines: from present work; dashed lines: from Ghia *et al.* (1982)

Figure 12.
Comparison of velocity profiles as predicted by 3D flow model against those by 2D flow model

	Re = 400		Re = 500		Re = 1,000	
	x_D	y_D	x_D	y_D	x_D	y_D
Ghia *et al.* (1982)	0.2617	0.3203	–	–	0.3034	0.3536
Iwatsu *et al.* (1989)	0.2604	0.2817	–	–	0.2623	0.2765
Pan and Acrivos (1967)	–	–	–	0.350	–	0.280
Koseff and Street (1984a)	–	–	–	–	–	0.316
Present	0.258	0.278	0.258	0.278	0.262	0.282

Notes: (x_D, y_D) are the vertical and horizontal extent, respectively, of the downstream-secondary eddy at the symmetry-plane $z = 0.5$ (for all cases, $A = 1$)

Table V.
Comparison for vertical and horizontal extent of the downstream-eddy size with 2D numerical and experimental results for a cubic cavity at Re = 400, 500 and 1,000

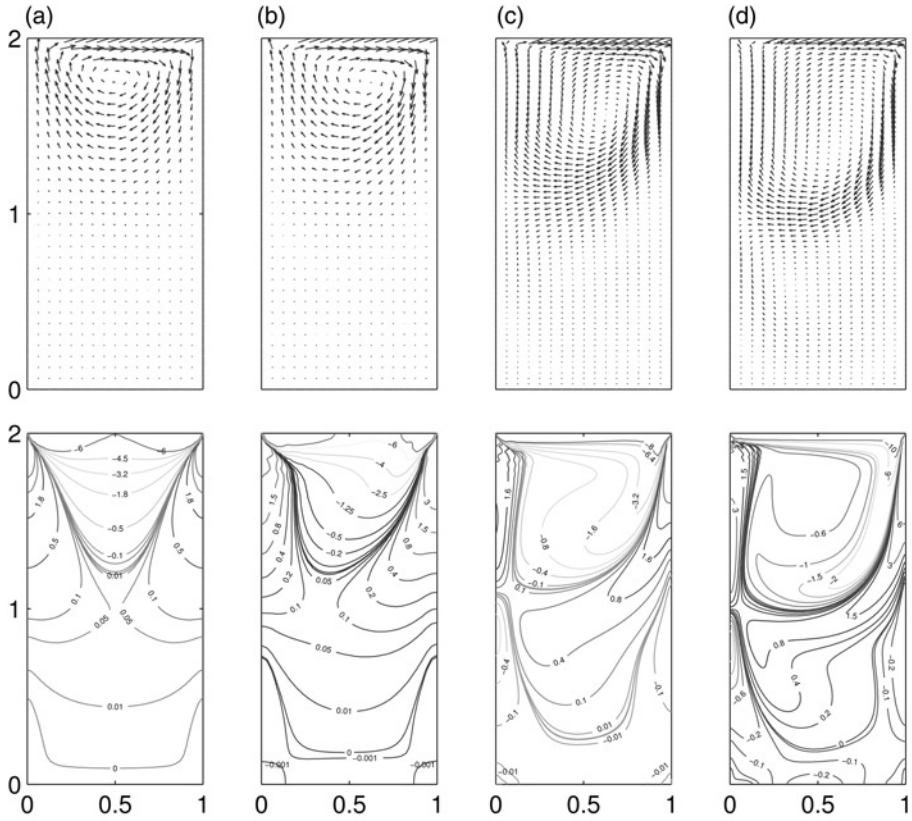

Notes: Aspectratios $A = 1$, $K = 2$; the abscissa and ordinate are same as in Figure 8.Reynolds numbers correspond to: (a) 0.01, (b) 100, (c) 400 and (d) 1,000, respectively. Velocity and vorticity components are the same as in Figure 8

Figure 13.
Plots of velocity vector (top row) and vorticity contour (bottom row)

of secondary-flow vortices appearing near the geometric center of the cavity (Figure 15(b)). For $K = 1$, we observe a distinct change in the structure of the flow-field. In the plane PP, a pair of secondary-flow vortices (Figure 16(a)) are found at small Reynolds number (around 0.01-100), that gradually shift towards the lower corner of the cavity side-walls with increasing Reynolds numbers (Figure 16(b) and (c)). Also, two pairs of longitudinal vortices begin to appear at the upper corner of the side-walls (in fact, a closer examination revealed the presence of a few other weak vortices, thus making the flow-field quite complex). These secondary vortices gain in strength with increase in Reynolds numbers (Figures 16(c)). For instance, at Re = 100, the vorticity component in the direction of lid-motion is found to have a magnitude of $\Omega_x = 0.3511$ for the secondary vortex, while the vorticity component $\Omega_z = 2.9213$ at the center of the primary vortex (see Table IV). However, at Re = 1,000, these components are found to be $\Omega_x = 2.6341$ and $\Omega_z = 0.6811$, respectively. For deep cavities, secondary flow was found to be insignificant near the bottom wall.

Summarized in Table VII are the results obtained with respect to the secondary vortex on the plane PP ($x = N_x/2$) at different Reynolds numbers for $K = A = 1$ cavity. Listed are the predicted values of the x-component of the most prominent

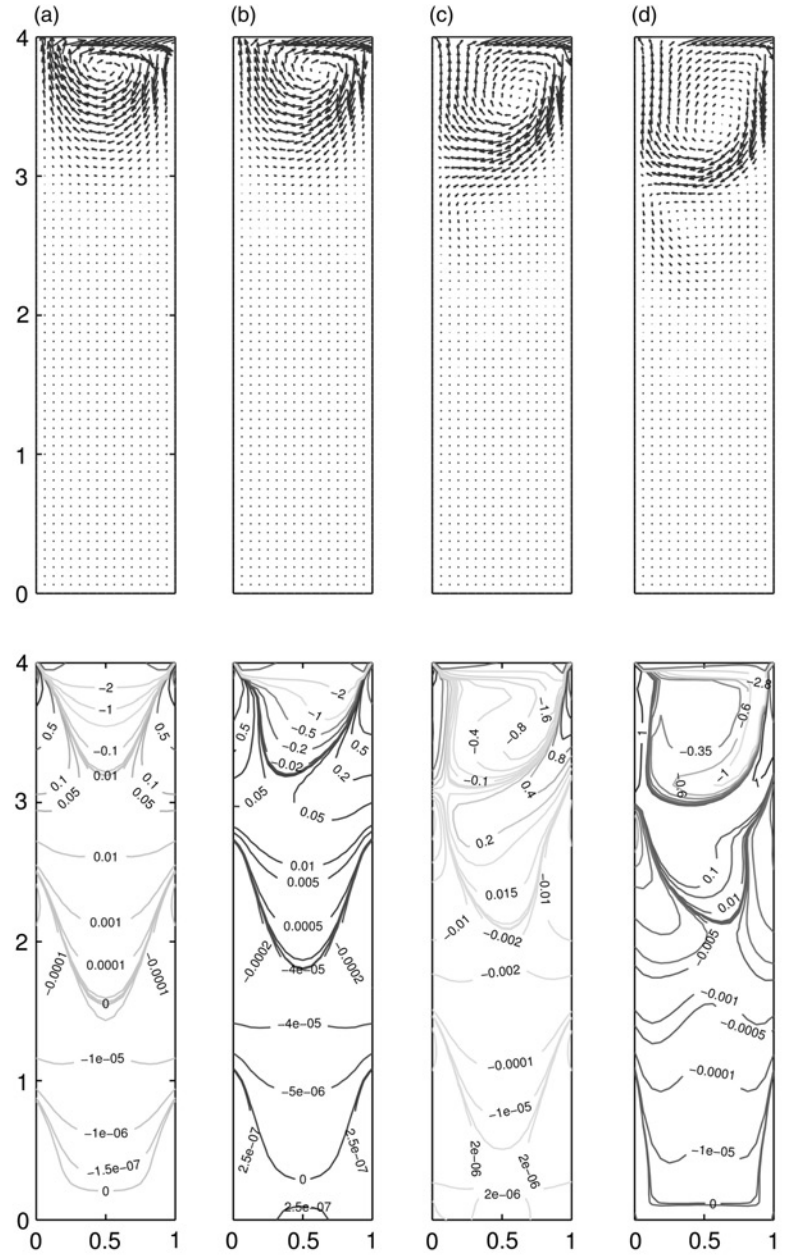

Figure 14.
Velocity vector (top row) and vorticity contour (bottom row) plot

Notes: Aspect ratios $A = 1$, $K = 4$; the abscissa and ordinate are same as in Figure 8. Reynolds numbers correspond to: (a) 0.01, (b) 100, (c) 400 and (d) 1000, respectively. Velocity and vorticity components are the same as in Figure 8

K	Re	First (x_c, y_c)	First Ω_c	Second (x_c, y_c)	Second Ω_c	Third (x_c, y_c)	Third Ω_c
1	0.01	(0.5, 0.22)	3.3743	–	–	–	–
	100	(0.614, 0.244)	2.9213	–	–	–	–
	400	(0.618, 0.428)	1.4043	–	–	–	–
	1,000	(0.591, 0.543)	0.6811	–	–	–	–
2	0.01	(0.5, 0.22)	3.3472	(0.5, 1.816)	−0.00184	–	–
	100	(0.614, 0.245)	2.8428	(0.62, 1.56)	−0.01056	–	–
	400	(0.622, 0.442)	1.4427	(0.462, 1.313)	−0.2985	–	–
	1,000	(0.608, 0.641)	0.7992	(0.357, 1.412)	−0.4346	–	–
4	0.01	(0.5, 0.224)	3.3432	(0.5, 1.87)	−0.0022	(0.5, 3.5)	1.164×10^{-6}
	100	(0.614, 0.245)	2.8373	(0.573, 1.595)	−0.0096	(0.496, 3.253)	4.440×10^{-6}
	400	(0.622, 0.442)	1.4408	(0.458, 1.318)	−0.2946	(0.492, 2.916)	2.128×10^{-4}
	1,000	(0.610, 0.645)	0.8134	(0.394, 1.349)	−0.4550	(0.484, 3.623)	1.678×10^{-4}

Notes: Here y_c is the distance from the moving lid and Ω_c is the z-component of vorticity at $(x_c, y_c, 0.5)$ (for all cases, $A = 1$)

Table VI.
Location of the center of the first, second and third primary vortex, at different aspect ratios (K) and Reynolds numbers

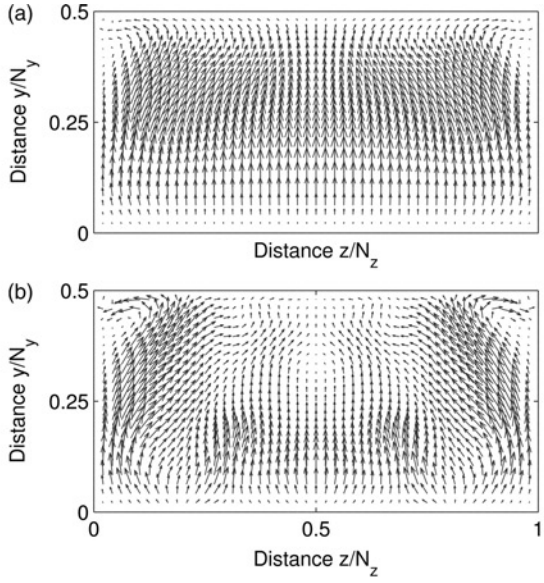

Note: The velocity components are in the plane of the paper (PP)

Figure 15.
Plots of velocity vector on the plane PP for aspect ratios $A = 1$, $K = 0.5$ at Reynolds numbers (a) Re = 400 and (b) Re = 1,000

secondary vortex, and the location of its center on the plane PP. It may be observed from Table VII that the secondary vortex becomes stronger and shifts downwards with increase in the Reynolds number. It was also observed that the strength of the primary vortex decreases with an increase in Reynolds numbers (see Table VII). Therefore, it may be concluded that the three-dimensionality of the flow induces a transfer of motion from the principal direction (namely, x) to the transverse direction, with increase in the Reynolds number. Plane 2D-simulations are unable to capture such a character of real flows. This feature could be related to the phenomenon of vortex stretching, which

leads to an intensification of local vorticity in 3D flows, but is absent in 2D flows (Batchelor, 1967).

4. Conclusions

In this paper, the lid-driven flow in 3D rectangular cavities has been investigated using MRT-LBM. The present numerical simulations not only validate the flow characteristics reported by previous researchers for lid-driven 3D flows in a cubic cavity ($K = 1$) with different Reynolds numbers, but also extend the results to flows in cavities with different aspect ratios.

Based on the investigations conducted for different sets of (K, Re), the following conclusions can be made. When $K \leq 1$, the vortex structure in the cavity changes considerably with Re. For $\mathrm{Re} \leq 100$, the flow structure inside the cavity is characterized by a large vortex filling almost the whole cavity. As Re increases, a second primary vortex appears beside the first primary vortex and the flow in the cavity becomes more complex. The major feature of the flow in a 3D deep cavity ($K > 1$) is that the entire cavity is filled with a series of counter-rotating primary vortices placed vertically along the cavity-height. The size, center position, vorticity and the number of vortices depends on both the Reynolds number and the cavity aspect ratio. It is further observed that the inertia force near the cavity-bottom decreases with increasing depth-to-width aspect ratio, and beyond a critical value of this ratio, flow characteristics there approach the theoretical limit of creeping flow.

The present simulations demonstrate that 2D models may predict the flow structure reasonably well at low Reynolds numbers, but significant differences appear at high Reynolds numbers. This discrepancy between 2D- and 3D-results are attributed to the effect of boundary layers near the side-walls in transverse direction (in 3D), due to

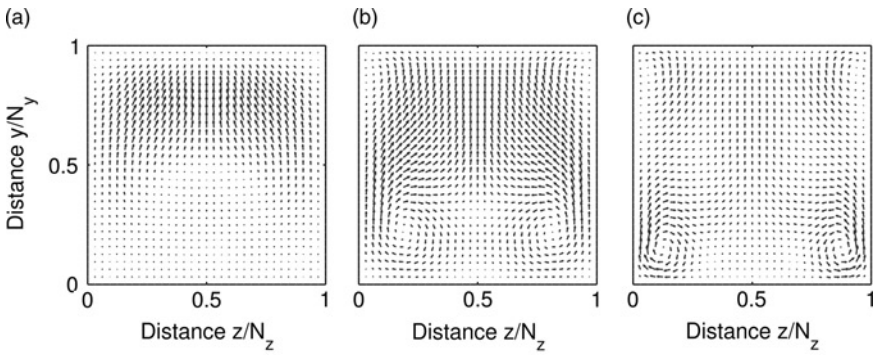

Note: The velocity components are in the plane of the paper (PP)

Figure 16.
Plots of velocity vector on the plane PP for aspect ratios $A = 1$, $K = 1$ at Reynolds numbers (a) $\mathrm{Re} = 0.01$, (b) $\mathrm{Re} = 400$ and (c) $\mathrm{Re} = 1{,}000$

Re	(y_c, z_c)	Ω_x
100	(0.62266, 0.68997)	−0.3511
400	(0.77857, 0.81394)	−1.2415
1,000	(0.85231, 0.87725)	−2.6341

Notes: Here y_c is the distance from the moving lid and Ω_x is the x-component of vorticity at $(0.5, y_c, z_c)$

Table VII.
Location and strength of the most prominent secondary vortex, at different Reynolds numbers ($K = A = 1$)

which the vorticity in the core-region is weakened in general. Also, owing to the vortex stretching effect present in 3D flow, the vorticity in the transverse plane intensifies whereas that in the lateral plane decays, with increase in Reynolds number. For high Reynolds numbers, strong secondary flow vortices whose axis is in the direction of the lid-motion are observed. Complex flow problems, such as, transition to turbulence, and turbulent flow in the cavities of different aspect ratios may be of interest for future studies.

References

Agrawal, A., Djenidi, L. and Antonia, R.A. (2005), "Simulation of gas flow in microchannels with a sudden expansion or contraction", *Journal of Fluid Mechanics*, Vol. 530, pp. 135-44.

Aidun, C.K., Triantafillopoulos, N.G. and Benson, J.D. (1991), "Global stability of a lid-driven cavity with throughflow flow visualization studies", *Physics of Fluids A*, Vol. 3 No. 9, pp. 2081-91.

Albensoeder, S. and Kuhlmann, H.C. (2005), "Accurate three-dimensional lid-driven cavity flow", *Journal of Computational Physics*, Vol. 206, pp. 536-58.

Albensoeder, S., Kuhlmann, H.C. and Rath, H.J. (2001), "Three-dimensional centrifugal-flow instabilities in the lid-driven-cavity problem", *Physics of Fluids*, Vol. 13 No. 1, pp. 121-35.

Alleborn, N., Raszillier, H. and Durst, F. (1999), "Lid-driven cavity with heat and mass transport", *International Journal of Heat and Mass Transfer*, Vol. 42 No. 5, pp. 833-53.

Babu, V. and Korpela, S. (1994), "Numerical solution of the incompressible three-dimensional Navier–Stokes equations", *Computers & Fluids*, Vol. 23, p. 675.

Batchelor, G.K. (1967), *An Introduction to Fluid Dynamics*, Cambridge University Press, Cambridge.

Bouzidi, M., Firdaouss, M. and Lallemand, P. (2001), "Momentum transfer of a Boltzmann-lattice fluid with boundaries", *Physics of Fluids*, Vol. 13, p. 3452.

Chen, S. and Doolen, G.D. (1998), "Lattice Boltzmann method for fluid flows", *Annual Review of Fluid Mechanics*, Vol. 30, p. 329.

Cheng, M. and Hung, K.C. (2006), "Vortex structure of steady flow in a rectangular cavity", *Computers & Fluids* Vol. 35, p. 1046.

Chew, Y.T., Shu, C. and Niu, X.D. (2002), "A new differential lattice Boltzmann equation and its application to simulate incompressible flows on non-uniform grids", *Journal of Statistical Physics*, Vol. 107 No. 112, p. 329.

Chiang, T., Sheu, W. and Hwang, R. (1998), "Effect of Reynolds number on the eddy structure in a lid-driven cavity", *International Journal of Numerical Methods in Fluids*, Vol. 26, p. 557.

Cortes, A.B. and Miller, J.D. (1994), "Numerical experiments with the lid driven cavity flow problem", *Computers & Fluids*, Vol. 23 No. 8, pp. 1005-27.

Das, M.K. and Kanna, P.R. (2007), "Application of an ADI scheme for steady and periodic solutions in a lid-driven cavity problem," *International Journal of Numerical Methods for Heat & Fluid Flow*, Vol. 17 No. 8, pp. 799-822.

De Vahl Davis, G. and Mallinson, G.D. (1976), "An evaluation of upwind and central difference approximations by a study of recirculating flow", *Computers & Fluids*, Vol. 4, p. 29.

d'Humières, D. (1992), "Generalized lattice Boltzmann equations", in Shizgal, B.D. and Weaver, D.P. (Eds), *Rarefied Gas Dynamics: Theory and Simulations, Progress Aeronautics and Astronautics*, Vol. 159, p. 450.

d'Humières, D., Ginzburg, I., Krafczyk, M., Lallemand, P. and Luo, L.S. (2002), "Multiple-relaxation-time lattice Boltzmann models in three dimensions", *Philosophical Transactions of Royal Society of London A*, Vol. 360, p. 437.

Ghia, U., Ghia, K.N. and Shin, C.T. (1982), "High-Re solutions of incompressible Navier–Stokes equations by coupled strongly implicit multigrid method", *Journal of Computational Physics*, Vol. 48, p. 387.

Ginzbourg, I. and Adler, P.M. (1994), "Boundary flow condition analysis for the three-dimensional lattice Boltzmann model", *Journal of Physics II*, Vol. 4, pp. 191.

Guo, Z., Shi, B. and Wang, N. (2000), "Lattice BGK model for incompressible Navier–Stokes equation", *Journal of Computational Physics*, Vol. 165, p. 288.

Gustafson, K. and Halasi, A. (1986), "Vortex dynamics of cavity flows", *Journal of Computational Physics*, Vol. 64, pp. 279-319.

He, X., Zou, Q., Luo, L.S. and Dembo, G. (1997), "Analytic solutions and analysis on non-slip boundary condition for the lattice Boltzmann BGK model", *Journal of Statistical Physics*, Vol. 87, p. 115.

Huang, H., Lee, T.S. and Shu, C. (2005), "Lattice-BGK simulation of steady flow through vascular tubes with double constrictions", *International Journal of Numerical Methods for Heat & Fluid Flow*, Vol. 16 No. 2, pp. 185-203.

Huang, H., Lee, T.S. and Shu, C. (2006), "Lattice Boltzmann method simulation gas slip flow in long microtubes", *International Journal of Numerical Methods for Heat & Fluid Flow*, Vol. 17 No. 6, pp. 587-607.

Iwatsu, R., Ishii, K., Kawamura, T., Kuwahara, K. and Hyun, J. (1989), "Numerical simulation of three-dimensional flow structure in a driven cavity", *Fluid Dynamics Research*, Vol. 5, p. 173.

Jana, S.C., Metcalfe, G. and Ottino, J.M. (1994), "Experimental and numerical studies of mixing in complex Stokes flow: the vortex mixing flow and multicellular cavity flow", *Journal of Fluid Mechanics*, Vol. 269, pp. 199-246.

Koseff, J.R. and Street, R.L. (1984a), "Visualization studies of a shear driven three-dimensional recirculating flow", *Journal of Fluid Engineering*, Vol. 106, p. 21.

Koseff, J.R., and Street, R.L. (1984b), "On end wall effects in a lid-driven cavity flow", *Journal of Fluids Engineering*, Vol. 106, p. 385.

Koseff, J.R. and Street, R.L. (1984c), "The lid-driven cavity flow: a synthesis of qualitative and quantitative observations", *Journal of Fluids Engineering*, Vol. 106, p. 390.

Ku, H.C., Hirsh, R.S. and Taylor, T.D. (1987), "A Pseudospectral method for solution of the three-dimensional incompressible Navier–Stokes equations", *Journal of Computational Physics*, Vol. 70, p. 439.

Lallemand, P. and Luo, L.S. (2000), "Theory of the lattice Boltzmann method: dispersion, dissipation, isotropy, Galilean invariance and stability". *Physical of Review E*, Vol. 61, p. 6546.

Lallemand, P. and Luo, L.S. (2003), "Theory of the lattice Boltzmann method: acoustic and thermal properties in two and three dimensions", *Physical of Review E*, Vol. 68, p. 036706.

Latt, J. and Chopard, B. (2006), "Lattice Boltzmann method with regularized pre-collision distribution functions", *Mathematics and Computers in Simulation*, Vol. 72, p. 165.

Leriche, E. and Gavrilakis, S. (2000), "Direct numerical simulation of the flow in a lid-driven cubical cavity", *Physics of Fluids*, Vol. 12, p. 1363.

Lu, Z., Liao, Y., Qian, D., McLaughlin, J.B., Derksen, J.J. and Kontomaris, K. (2002), "Large eddy simulations of a stirred tank using the lattice Boltzmann method on a nonuniform grid", *Journal of Computational Physics*, Vol. 181, p. 675.

Mills, R.D. (1965), "On the close motion of a fluid in a square cavity", *Journal of the Royal Aeronautical Society*, Vol. 69, p. 116.

Pan, F. and Acrivos, A. (1967), "Steady flows in rectangular cavities", *Journal of Fluid Mechanics*, Vol. 28, pp. 643-655.

Patil, D.V., Lakshmisha, K.N. and Rogg, B. (2006), "Lattice Boltzmann simulation of lid-driven flow in deep cavities", *Computers Fluids*, Vol. 35, p. 1116.

Qian, Y.H., d'Humières, D. and Lallemand, P. (1992), "Lattice BGK models for Navier–Stokes equation", *Europhysics Letters*, Vol. 17 No. 6, p. 479.

Schreiber, R. and Keller, H.B. (1983), "Driven cavity flows by effective numerical techniques", *Journal of Computational Physics*, Vol. 49, p. 310.

Shankar, P.N. (1993), "The eddy structure in Stokes flow in a cavity", *Journal of Fluid Mechanics*, Vol. 250, p. 371.

Shankar, P.N. and Deshpande, M.D. (2000), "Fluid Mechanics in the driven cavity", *Annual Review of Fluid Mechanics*, Vol. 32, p. 93-136.

Shen, C. and Floryan, J.M. (1985), "Low Reynolds number flow over cavities", *Physics of Fluids*, Vol. 28, p. 3191.

Shuja, S.Z., Yilbas, B.S. and Iqbal, M.O. (2000), "Mixed convection in a square cavity due to heat generating rectangular body effect of cavity exit port locations", *International Journal of Numerical Methods for Heat & Fluid Flow*, Vol. 10 No. 8, pp. 824-41.

Succi, S. (2001), *The Lattice Boltzmann Equation for Fluid Dynamics and Beyond*. Oxford University Press, Oxford.

Wong, J.C.F. (2007), "Numerical simulation of two-dimensional laminar mixed-convection in a lid-driven cavity using the mixed finite element consistent splitting scheme", *International Journal of Numerical Methods for Heat & Fluid Flow*, Vol. 17 No. 1, pp. 46-93.

Yu, D., Mei, R., Luo, L.-S. and Shyy, W. (2003), "Viscous flow computations with the method of lattice Boltzmann equation", *Progress in Aerospace Sciences*, Vol. 39, pp. 329-67.

Ziegler, D.P. (1993), "Boundary conditions for lattice Boltzmann simulations", *Journal of Statistical Physics*, Vol. 71, p. 1171.

Corresponding author
K.N. Lakshmisha can be contacted at: knl@aero.iisc.ernet.in